Available Online: 5 November 2026 DOI: 10.54254/2977-3903/2026.38764

Structural design and simulation-based optimization of a PCB-stator axial-flux electromagnetic rotary actuator for fuze safety-and-arming mechanisms

Yang Li, Shuangjie Liu, Yachao Zhang, Zheyu Fang, Rui Guo*

School of Equipment Engineering, Shenyang Ligong University, Shenyang, China

*Corresponding Author. Email:ly79983867@163.com

Abstract. Conventional fuze Safety-and-Arming (S&A) mechanisms often rely on setback or centrifugal forces, whereas electrically driven pin pullers and motor–lead-screw units may require relatively long axial travel. This study presents a Printed Circuit Board (PCB)-stator axial-flux electromagnetic rotary actuator designed to switch between functional positions through 180° rotor rotation while retaining a potential reverse-drive path. The investigation focuses on the electromagnetic drive subsystem rather than the complete S&A mechanism. An electromechanical model was established using the voltage balance, back electromotive force, torque–current relation, rotor inertia, and equivalent resisting torque. A three-dimensional transient finite-element model was used to evaluate the effects of air gap and permanent-magnet thickness on 180° positioning time. The spatial magnetic-field distribution, friction-related resistance, and eddy-current losses were considered when interpreting the results. Within the investigated air-gap range of 0.5–1.1 mm, the shortest positioning time in the air-gap sweep was 45.0 ms at 1.1 mm. With this gap fixed, a magnet thickness of 1.2 mm yielded a finite-element positioning time of 42.6 ms, compared with 40.3 ms from the analytical model (a 5.40% difference relative to the finite-element result). A simplified prototype reached 180° in 35.8 ms at 5 A, compared with 33.98 ms from a simulation using the corresponding low-friction boundary conditions (a 5.08% difference relative to the measured time). These results support the drive model under the tested conditions; full-device locking, release, reverse recovery, and cyclic reliability remain to be verified.

Keywords: PCB-stator actuator, axial-flux permanent-magnet machine, electromechanical modeling, finite-element analysis, dynamic response

1. Introduction

Safety-and-Arming (S&A) mechanisms isolate and align the functional elements of a fuze. Conventional mechanisms commonly rely on setback or centrifugal forces, which can limit available actuation margin under low environmental acceleration. Research on Microelectromechanical-System (MEMS) S&A devices has examined miniaturized barriers, interlocking structures, and integrated actuation functions [1-3]. Subsequent simulation and experimental studies have considered structural reliability, setback-device fabrication, and

Copyright: © 2026 by the authors. Submitted for possible open access publication under the terms and conditions of the Creative Commons Attribution (CC BY) license (https://creativecommons.org/licenses/by/4.0/).

condition feedback, demonstrating that compactness must be considered together with predictable state transition and verification [4-7].

Electromagnetic actuation has also been investigated through microcoils and recoverable bistable mechanisms [8-10]. The output topology affects packaging: linear pin-puller architectures provide translation directly, whereas motor–lead-screw drives convert rotation into translation through an additional transmission path. A rotary output may reduce the required linear travel, provided that the required angular movement and final positioning can be achieved.

Printed Circuit Board (PCB) stator windings offer planar fabrication and repeatable conductor geometry. Studies have compared PCB winding topologies, demonstrated optimized PCB axial-flux machines, and investigated eddy-current and circulating-current losses [11-13]. Recent reviews of axial-flux permanent-magnet machines and a study of a double-PCB-stator configuration also emphasize compact axial packaging and the need for three-dimensional magnetic-field analysis [14, 15]. These developments provide a technical basis for examining a PCB-stator rotary actuator, although motor performance results cannot by themselves validate a complete fuze S&A mechanism.

This study proposes a PCB-stator axial-flux electromagnetic rotary actuator and investigates its drive subsystem through analytical modeling, three-dimensional transient finite-element analysis, and a simplified prototype test. The contributions are threefold: (1) a rotary architecture designed to use 180° angular displacement for functional-position alignment while retaining a possible reverse-drive path; (2) an electromechanical model combined with a parameter study of air gap and permanent-magnet thickness; and (3) experimental comparison of measured and simulated positioning times under a matching low-friction boundary. The tests do not establish full-device spring locking, axial release, reverse recovery, or cyclic reliability.

2. Actuator configuration and dynamic model

2.1. Structural concept and operating sequence

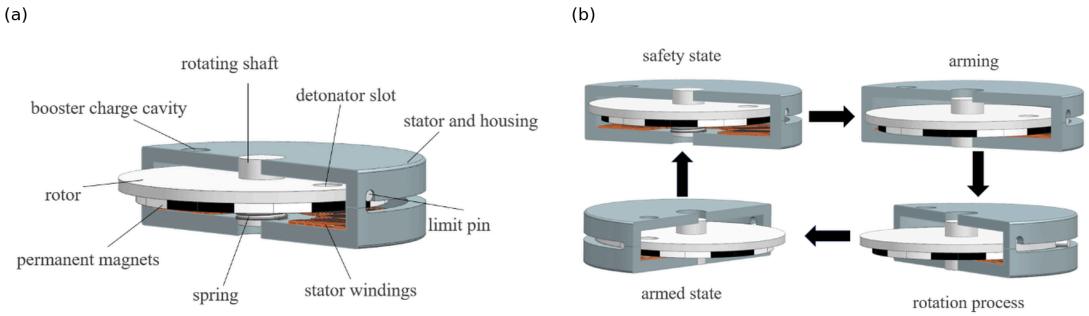


Figure 1. Structural layout and intended operating sequence of the proposed actuator: (a) component arrangement; (b) conceptual state-transition sequence

The proposed actuator consists of a rotor, permanent magnets, a PCB stator winding, a rotating shaft, a housing, a spring, and a limiting pin. Figure 1(a) shows the component arrangement. In the intended full mechanism, a pin-and-groove restraint defines the initial safe position. Energizing the winding is intended to release the restraint and generate torque that rotates the rotor through 180°, changing the alignment of the functional passages. The design also retains a possible reverse-drive path. Figure 1(b) illustrates the intended

state-transition sequence; it should be interpreted as a structural concept rather than evidence of experimentally demonstrated recovery.

The prototype reported in this study was simplified by omitting the reset spring and integrating the rotor with the shaft to reduce contact friction. Accordingly, the experimental scope is limited to forward rotary positioning of the electromagnetic drive subsystem. The full restraint-release sequence and the return to the safe position require separate tests on the complete assembly.

2.2. Electromechanical dynamic model

The rotating stage was represented as a compact Brushless Direct-Current (BLDC) drive. Under the simplifying assumption that winding inductance is negligible over the startup interval, the voltage balance is [16, 17]:

$$U = Ri + K_e\omega \tag{1}$$

The electromagnetic torque is approximated as proportional to current:

$$T_e = K_t i \tag{2}$$

The rotor dynamics and angular displacement are described by the following relationships:

$$J\frac{d\omega}{dt} = T_e - T_r \tag{3}$$

$$\theta(t) = \int_0^t \omega(\tau)\, d\tau \tag{4}$$

Here, U and i denote the applied voltage and current; R is the effective circuit resistance; K_e and K_t are the back-electromotive-force and torque constants; ω is angular velocity; θ is angular displacement (in radians in the governing equation, with 180° = π rad); J is rotor inertia; T_e is electromagnetic torque; and T_r is the equivalent resisting torque. For a voltage-fed interval, substituting $i = (U - K_e\omega)/R$ into the mechanical equation gives:

$$J\frac{d\omega}{dt} = \frac{K_t}{R}\left(U - K_e\omega\right) - T_r \tag{5}$$

The analytical representation links electrical input to the angular response. It assumes a simplified magnetic circuit and groups bearing/contact friction and other resisting effects into T_r; spatial field nonuniformity and parameter-dependent losses are examined in the three-dimensional finite-element model. Equation (5) applies to a voltage-fed interval; for current-controlled operation, the mechanical equation in (3) is evaluated using the prescribed current input. The principal response metric is the time required for θ to reach π rad (180°).

3. Finite element analysis and parameter effects

3.1. Model setup and evaluation criteria

A three-dimensional transient finite-element model was established for the stator, rotor, permanent magnets, and PCB windings. The slot–pole configuration was held fixed so that the effects of air gap and magnet thickness could be examined within a consistent model. The principal dimensions and excitation condition are summarized in Table 1, and the finite-element geometry and mesh are shown in Figure 2. The main response variable was the 180° positioning time; resisting torque, eddy-current losses, and axial magnetic-flux-density distribution were also considered when interpreting the response.

Table 1. Principal parameters of the electromagnetic drive model

Parameter	Value	Parameter	Value
Stator outer diameter, D_s	50 mm	Rotor outer diameter, D_r	48 mm
Stator inner diameter, d_s	20 mm	Rotor inner diameter, d_r	16 mm
Stator axial length	2 mm	Rotor axial length	2 mm
Turns per slot, N	20 turns	Reference current, I_0	5 A

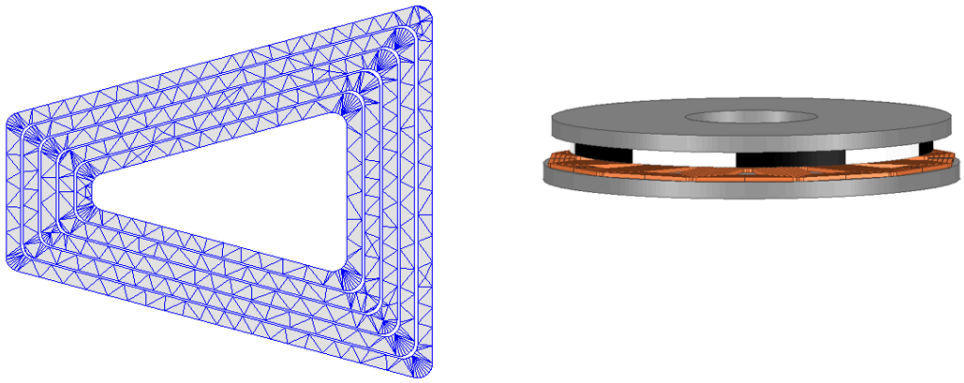


Figure 2. Three-dimensional finite-element model and mesh of the electromagnetic actuator

3.2. Effects of air gap and permanent-magnet thickness

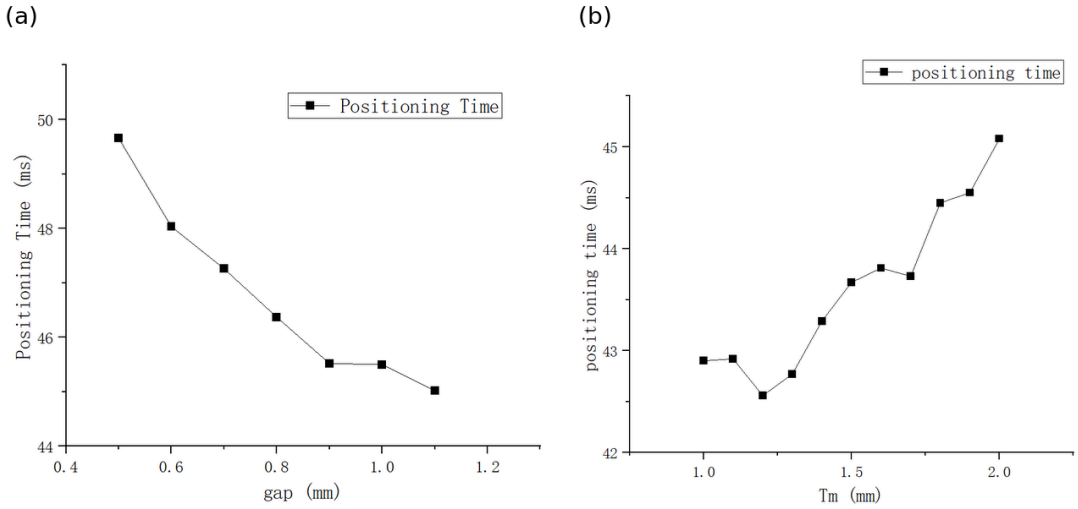


Figure 3. Effects of (a) air gap and (b) permanent-magnet thickness on 180° positioning time

The air gap affects both magnetic coupling and the resistance opposing rotor motion. A smaller gap generally strengthens magnetic interaction, but it can also increase axial magnetic attraction and the frictional load transmitted through contact interfaces. Time-varying fields additionally produce eddy-current losses. Thus, positioning time depends on the balance between electromagnetic drive and resisting effects rather than on torque magnitude alone. Across the investigated air-gap interval of 0.5–1.1 mm, positioning time decreased

overall and reached 45.0 ms at 1.1 mm (Figure 3(a)). This result is limited to the tested interval and should not be extrapolated to larger gaps.

With the air gap fixed at 1.1 mm, magnet-thickness variation produced a nonmonotonic response (Figure 3(b)). Increasing magnet thickness can improve magnetic loading, while the accompanying increase in rotor mass and inertia can oppose acceleration. The shortest positioning time in this sweep was 42.6 ms at a magnet thickness of 1.2 mm. The air-gap result of 45.0 ms and the subsequent 42.6 ms result correspond to consecutive stages of the parameter study, not identical configurations.

3.3. Analytical comparison and magnetic-field results

At an air gap of 1.1 mm and a magnet thickness of 1.2 mm, the finite-element model predicted a positioning time of 42.6 ms, compared with 40.3 ms from the analytical model. The analytical prediction was 5.40% lower than the finite-element result, using the latter as the reference. As shown in Figure 4(a), the angular-displacement curves followed similar trends before reaching the target angle. Under the initial 5 A step-current input, the finite-element model predicted a peak electromagnetic torque of approximately 77.13 mN·m.

The three-dimensional axial magnetic-flux-density distribution in Figure 4(b) is spatially nonuniform. This supports using the finite-element model alongside the simplified analytical representation: the analytical assumptions do not resolve local field variation, leakage, and eddy-current effects in the same detail. The comparison supports the analytical model as a tool for estimating response trends under the studied conditions, while the finite-element result remains the basis for the reported optimized positioning time.

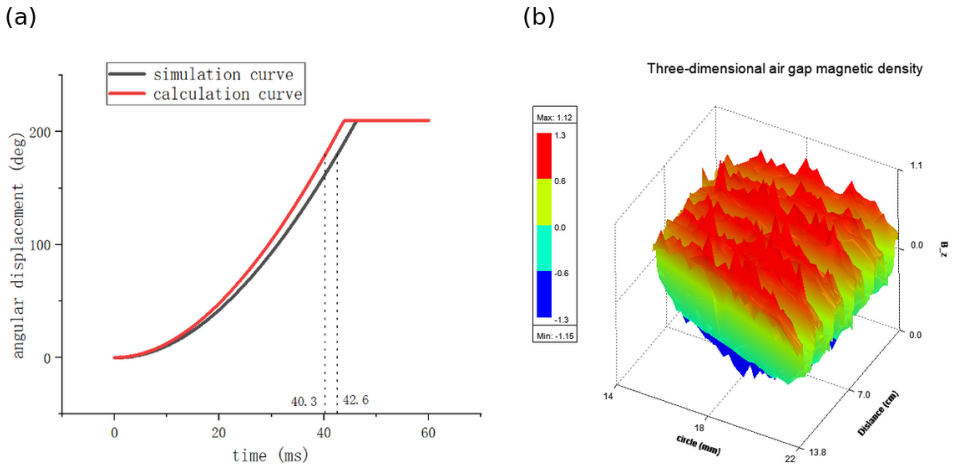


Figure 4. Results for the selected parameters: (a) analytical and finite-element angular-displacement responses; (b) three-dimensional axial magnetic-flux-density distribution

4. Prototype testing and model verification

4.1. Prototype and PCB winding characterization

A simplified prototype was manufactured to assess the rotary-drive response. The test unit had an outer diameter of 52 mm, an overall thickness of 11.6 mm, a 1.1 mm air gap, and a 12-slot, five-pole-pair configuration. NdFeB permanent magnets (grade NdFe35) were mounted with alternating north and south poles. The stator and rotor were resin-printed, the reset spring was omitted, and the rotor and shaft were integrated to reduce alignment error and friction variation. Figure 5 shows the PCB winding, assembled

prototype, and test setup. These simplifications were chosen to align the test boundary with the low-friction simulation rather than to validate the complete S&A mechanism.

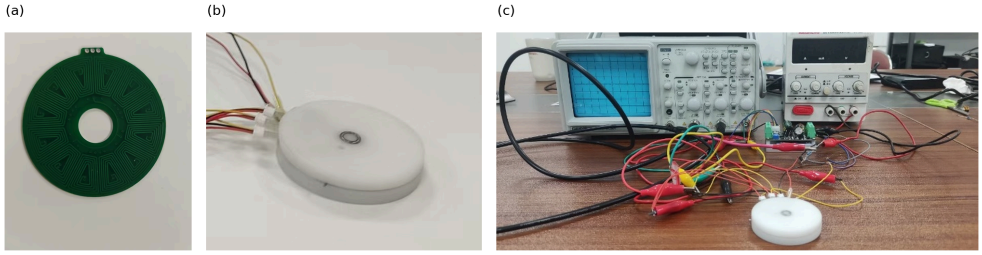


Figure 5. Prototype validation setup: (a) PCB stator winding; (b) assembled prototype; (c) dynamic-response test platform

Five PCB winding samples were measured at low direct-current voltage to limit heating-related resistance drift. The A–B, A–C, and B–C two-phase series resistances are listed in Table 2. All reported values were within 12.625–12.820 Ω, indicating a narrow resistance spread across these samples under the stated measurement conditions.

Table 2. Measured two-phase series resistance of five PCB winding samples

Sample	A–B resistance (Ω)	A–C resistance (Ω)	B–C resistance (Ω)
1	12.625	12.820	12.625
2	12.660	12.820	12.660
3	12.660	12.660	12.625
4	12.625	12.820	12.625
5	12.625	12.660	12.820

4.2. Dynamic response and model verification

The test platform used a regulated DC power supply, control electronics, a sampling resistor, and an oscilloscope. The voltage across the sampling resistor was recorded to track drive current. When the rotor reached the mechanical stop, the back electromotive force decreased and the current waveform changed; this transient was used to identify the completion time of the 180° movement. Each current condition was tested nine times, and the mean positioning time was reported.

Positioning time decreased as the drive current increased from 1 to 5 A (Figure 6(a)), although the reduction became smaller at higher currents. At 5 A, the measured positioning time was 35.8 ms. A simulation using the corresponding low-friction boundary conditions predicted 33.98 ms, giving a relative difference of 5.08% when the measured time is used as the reference (Figure 6(b)). This comparison must be distinguished from the 42.6 ms result obtained during structural-parameter optimization, because the two simulations used different resistance and friction boundaries.

The prototype also included two Hall sensors mounted 24° apart. Previous studies have shown that Hall-sensor misalignment can affect commutation timing in BLDC drives [18-20]. However, the endpoint time reported here was inferred from the current transient rather than directly from the Hall outputs. The 5.08% difference therefore supports the dynamic model only for the simplified low-friction drive subsystem and the stated endpoint-detection method; it does not establish the accuracy of the complete position-feedback sequence, spring locking, axial release, reverse recovery, or repeated-cycle reliability.

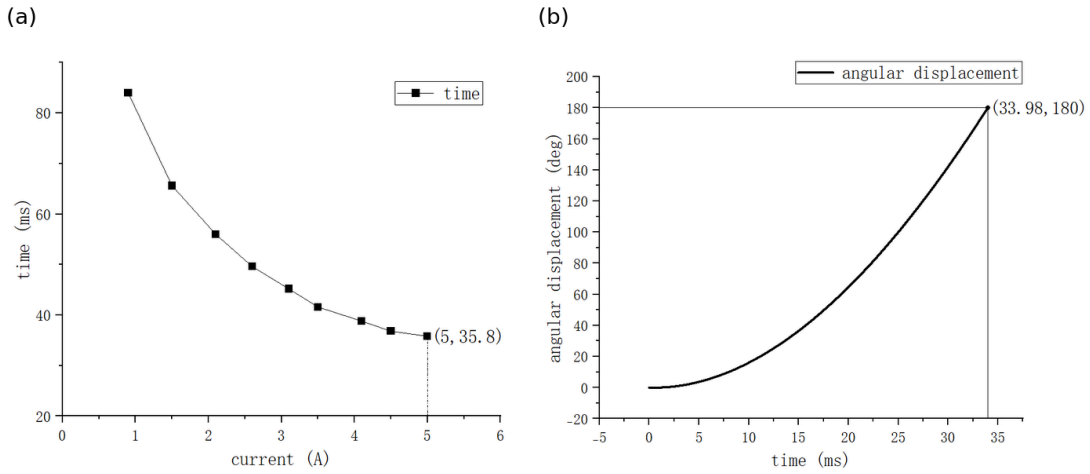


Figure 6. Dynamic-response results: (a) measured positioning time versus drive current; (b) simulated angular displacement under the low-friction test boundary

5. Conclusions

A PCB-stator axial-flux electromagnetic rotary actuator was proposed to replace a long linear actuation path with 180° rotary positioning while retaining a possible reverse-drive path. A simplified electromechanical model was combined with three-dimensional transient finite-element analysis to examine the effects of air gap and permanent-magnet thickness. Within the investigated design space, an air gap of 1.1 mm gave the shortest positioning time in the air-gap sweep (45.0 ms), and a subsequent magnet-thickness sweep identified 1.2 mm as the best tested thickness, with a positioning time predicted by finite-element analysis of 42.6 ms.

The analytical model predicted 40.3 ms for the selected configuration, 5.40% below the finite-element result when the latter is used as the reference. Under the low-friction prototype boundary conditions, the measured positioning time at 5 A was 35.8 ms, compared with 33.98 ms in simulation; this corresponds to a 5.08% relative difference when the measured time is used as the reference. These comparisons support the model for forward positioning of the electromagnetic drive subsystem under the conditions examined. Because the prototype omitted the reset spring and reduced contact friction, full-device locking, axial release, reverse restoration, and cyclic reliability remain unverified and should be evaluated using the complete assembly.

References

[1] Li, M., & Hu, T. (2021). Research status and development trend of MEMS S&A devices: A review. *Defence Technology, 17*(2), 450–456. https://doi.org/10.1016/j.dt.2020.02.014

[2] Rehan, M., & Mansoor, M. (2021). Application of MEMS in safety and arming devices: An overview. *Microsystem Technologies, 27*, 3599–3610. https://doi.org/10.1007/s00542-020-05162-4

[3] Wang, D., Lou, W., Feng, Y., & Zhang, X. (2017). Design of high-reliability micro safety and arming devices for a small caliber projectile. *Micromachines, 8*(8), Article 234. https://doi.org/10.3390/mi8080234

[4] Qin, Y., Shen, Y., Zou, X., & Hao, Y. (2022). Simulation and test of a MEMS arming device for a fuze. *Micromachines, 13*(8), Article 1161. https://doi.org/10.3390/mi13081161

[5] Qin, Y., Shen, Y., Zou, X., & Hao, Y. (2022). Test and improvement of a fuze MEMS setback arming device based on the EDM process. *Micromachines, 13*(2), Article 292. https://doi.org/10.3390/mi13020292

[6] Hu, T., Ren, W., Zhao, Y., & Xue, Y. (2019). The research on actuation performance of MEMS safety-and-arming device with interlock mechanism. *Micromachines, 10*(2), Article 76. https://doi.org/10.3390/mi10020076

[7] Wang, K., Hu, T., Zhao, Y., Ren, W., & Wang, Y. (2023). Design of an intelligent MEMS safety and arming device with a condition feedback function. *Micromachines, 14*(6), Article 1130. https://doi.org/10.3390/mi14061130

[8] Sun, Y., Lou, W., Feng, H., & Zhao, Y. (2020). Study on characteristics of electromagnetic coil used in MEMS safety and arming device. *Micromachines, 11*(8), Article 749. https://doi.org/10.3390/mi11080749

[9] Lv, S., Feng, H., Lou, W., Xiao, C., Su, W., Kan, W., & He, B. (2023). Research on the application of microcast electromagnetic coil in an Si MEMS bistable recoverable safety and arming device. *Micromachines, 14*(7), Article 1346. https://doi.org/10.3390/mi14071346

[10] Fan, X., Hu, T., Wang, Y., Zhao, Y., Tian, Z., & Xue, W. (2024). Research on multiphysics-driven MEMS safety and arming devices. *Micromachines, 15*(10), Article 1194. https://doi.org/10.3390/mi15101194

[11] Tokgöz, F., Çakal, G., & Keysan, O. (2020). Comparison of PCB winding topologies for axial-flux permanent magnet synchronous machines. *IET Electric Power Applications, 14*(13), 2577–2586. https://doi.org/10.1049/iet-epa.2020.0622

[12] Tokgöz, F., Çakal, G., & Keysan, O. (2020). Design and implementation of an optimized printed circuit board axial-flux permanent magnet machine. In *2020 International Conference on Electrical Machines (ICEM)* (pp. 111–116). IEEE. https://doi.org/10.1109/ICEM49940.2020.9271058

[13] Chulaee, Y., Heins, G., Robinson, B., Mohammadi, A., Thiele, M., Patterson, D., & Ionel, D. M. (2024). Design and optimization of high-efficiency coreless PCB stator axial flux PM machines with minimal eddy and circulating current losses. *IEEE Transactions on Industry Applications, 60*(6), 8722–8735. https://doi.org/10.1109/TIA.2024.3447620

[14] Nishanth, F. N. U., Van Verdeghem, J., & Severson, E. L. (2023). A review of axial flux permanent magnet machine technology. *IEEE Transactions on Industry Applications, 59*(4), 3920–3933. https://doi.org/10.1109/TIA.2023.3258933

[15] Li, Y., Gao, J., Wu, D., Deng, Z., Wang, G., Zhang, J., & Zheng, X. (2025). The electromagnetic characteristics analysis and the control of a new axial flux permanent magnet machine with a double-PCB stator. *Review of Scientific Instruments, 96*(8), Article 084704. https://doi.org/10.1063/5.0278731

[16] Gerada, D., Mebarki, A., Brown, N. L., Gerada, C., Cavagnino, A., & Boglietti, A. (2014). High-speed electrical machines: Technologies, trends, and developments. *IEEE Transactions on Industrial Electronics, 61*(6), 2946–2959. https://doi.org/10.1109/TIE.2013.2286777

[17] Vaez-Zadeh, S. (2018). *Control of permanent magnet synchronous motors*. Oxford University Press. https://doi.org/10.1093/oso/9780198742968.001.0001

[18] Zhang, Q., & Feng, M. (2018). Combined commutation optimisation strategy for brushless DC motors with misaligned Hall sensors. *IET Electric Power Applications, 12*(3), 301–307. https://doi.org/10.1049/iet-epa.2017.0276

[19] Hung, C. W., & Hsu, C. L. (2016). A simulation model of Hall sensor misalignment in BLDC motors. *Journal of Robotics, Networking and Artificial Life, 3*(3), 152–157. https://doi.org/10.2991/jrnal.2016.3.3.4

[20] Al-Adsani, A. S., AlSharidah, M. E., & Beik, O. (2021). BLDC motor drives: A single Hall sensor method and a 160° commutation strategy. *IEEE Transactions on Energy Conversion, 36*(3), 2025–2035. https://doi.org/10.1109/TEC.2020.3046183